Mon. Not. R. Astron. Soc. **000**, 1–17 (2002) Printed 9 March 2016 (MN LATEX style file v2.2)

MHD simulation of the formation of clumps and filaments in quiescent diffuse medium by thermal instability

C. J. Wareing[1⋆], J. M. Pittard[1], S. A. E. G. Falle[2] and S. Van Loo[1]
[1]*School of Physics and Astronomy, University of Leeds, Leeds, LS2 9JT, U.K.*
[2]*School of Mathematics, University of Leeds, Leeds, LS2 9JT, U.K.*

arXiv:1601.04361v2 [astro-ph.GA] 8 Mar 2016

Accepted 2016 March 08. Received 2016 March 01; in original form 2016 January 15

ABSTRACT

We have used the AMR hydrodynamic code, MG, to perform idealised 3D MHD simulations of the formation of clumpy and filamentary structure in a thermally unstable medium without turbulence. A stationary thermally unstable spherical diffuse atomic cloud with uniform density in pressure equilibrium with low density surroundings was seeded with random density variations and allowed to evolve. A range of magnetic field strengths threading the cloud have been explored, from $\beta = 0.1$ to $\beta = 1.0$ to the zero magnetic field case ($\beta = \infty$), where β is the ratio of thermal pressure to magnetic pressure. Once the density inhomogeneities had developed to the point where gravity started to become important, self-gravity was introduced to the simulation. With no magnetic field, clouds and clumps form within the cloud with aspect ratios of around unity, whereas in the presence of a relatively strong field ($\beta = 0.1$) these become filaments, then evolve into interconnected corrugated sheets that are predominantly perpendicular to the magnetic field. With magnetic and thermal pressure equality ($\beta = 1.0$), filaments, clouds and clumps are formed. At any particular instant, the projection of the 3D structure onto a plane parallel to the magnetic field, i.e. a line of sight *perpendicular* to the magnetic field, resembles the appearance of filamentary molecular clouds. The filament densities, widths, velocity dispersions and temperatures resemble those observed in molecular clouds. In contrast, in the strong field case $\beta = 0.1$, projection of the 3D structure along a line of sight *parallel* to the magnetic field reveals a remarkably uniform structure.

Key words: MHD – instabilities – ISM: structure – ISM: clouds – ISM: molecules – methods: numerical

1 INTRODUCTION

Extensive studies of the nearest star-forming clouds, most recently with the *Herschel* Space Observatory have revealed that every interstellar cloud contains an intricate network of interconnecting filamentary structures (see, for example, Section 2 of the review of André et al. (2014) and references therein). The data, from *Herschel* and near-IR studies for example, suggest a scenario in which these ubiquitous filaments represent a key step in the star formation process: large-scale flows compress the diffuse ISM and form molecular clouds; an interconnecting filamentary structure forms within these clouds; magnetic fields affect the directions of movement and hence overall structure, although do not appear to set the central densities in the filaments; gravity plays an increasingly important role, fragmenting the filaments once they are cold and dense into prestellar cores and finally protostars. Observational results now connect well with numerical simulations, as highlighted in Section 5 of André et al. (2014) and the references therein. Numerical simulations now include the thermodynamic behaviour of the cloud material, magnetic fields, gravity and feedback from massive stars, both radiative and dynamic. Turbulence has emerged as an ingredient which can, injected at the right scale, result in the formation of filaments which possess properties remarkably similar to those derived from observational results.

In the work presented here, we explore the formation of filaments through the use of MHD simulations of the thermal instability (Field 1965) in a low-density cloud of quiescent diffuse medium initially in the warm unstable phase and in pressure equilibrium with its lower-density surroundings, including accurate thermodynamics, magnetic fields and self-gravity. Our motivation is to study the underlying physics of the thermal instability under initially quiescent conditions, without additional complications such as driven turbulence

⋆ E-mail: C.J.Wareing@leeds.ac.uk

or colliding flows. In the next two sections, we review recent relevant results, summarising properties of filaments derived from observational results in Section 2 and recent relevant work on analytical and numerical filament formation models in Section 3. In Section 4 we present our numerical method and define the initial conditions used in our model. In Section 5 we present our results and in Section 6 analyse those results with comparison with the observational results discussed in Section 2. We conclude the work in Section 7.

2 PROPERTIES OF FILAMENTS

Filaments and their importance for star formation have been noted by many authors for decades. We follow the review of André et al. (2014) and define filaments as any elongated ISM structures with an aspect ratio larger than ∼5-10 that are significantly overdense with respect to their surroundings. They are not thought to be projections of sheets or larger structures. Schneider & Elmegreen (1979) discussed the properties of elongated dark nebulae with internal structures they named "globular filaments". Within star-forming molecular gas, CO and dust observations revealed that both the Orion A cloud (e.g. Bally et al. 1987; Chini et al. 1997; Johnstone & Bally 1999) and the Taurus Cloud (e.g. Abergel et al. 1994; Mizuno et al. 1995; Hartmann 2002; Nutter et al. 2008; Goldsmith et al. 2008) have prominent filamentary structure. Other well-known examples include the molecular clouds in the constellations Musca and Chamaeleon (e.g. Cambrésy 1999), Perseus (e.g. Hatchell et al. 2005), and S106 (e.g. Balsara, Ward-Thompson & Crutcher 2001). After making comparisons, Myers (2009) noted that young stellar groups and clusters are frequently associated with dense "hubs" radiating multiple lower-column-density filaments.

The *Herschel* Space Observatory has now uncovered filamentary structure in molecular clouds and infrared dark clouds in great detail (see the review of André et al. (2014) and also, for example, André et al. (2010), Könyves et al. (2010), Arzoumanian et al. (2011, 2013), Peretto et al. (2012), Schneider et al. (2012) and Palmeirim et al. (2013) for more detail). Notably, filamentary structure is present in every cloud observed with *Herschel*, independent of whether the cloud is actively star-forming or not. For example, the Polaris Flare, a translucent, non-star forming cloud is clearly filamentary in structure in both *Herschel*-derived column density and in 250 μm continuum emission (Ward-Thompson et al. 2010; Miville-Deschênes et al. 2010). This ubiquity indicates the formation of filaments precedes star formation in the cold ISM, and is tied to processes acting within clouds themselves (André et al. 2014).

The *Herschel* observations have revealed a number of interesting results regarding the properties of filaments. Most often noted is the result from detailed analysis of resolved filamentary column density profiles (e.g. Arzoumanian et al. 2011; Juvela et al. 2012; Palmeirim et al. 2013) that the shape of filament profiles is universal and described by a Plummer-like function of the form (Plummer 1911; Whitworth & Ward-Thompson 2001; Nutter et al. 2008; Arzoumanian et al. 2011):

$$\rho_p\left(r\right) = \frac{\rho_c}{\left[1+\left(r/R_{flat}\right)^2\right]^{p/2}} \tag{1}$$

for the density profile, equivalent to:

$$\Sigma_p\left(r\right) = A_p \frac{\rho_c R_{flat}}{\left[1+\left(r/R_{flat}\right)^2\right]^{\frac{p-1}{2}}} \tag{2}$$

for the column density profile, where ρ_c is the central density of the filament, R_{flat} is the radius of the flat inner region, $p \approx 2$ is the power-law exponent at large radii ($r >> R_{flat}$), and A_p is a finite constant factor which includes the effect of the filament's inclination angle to the plane of the sky. It is notable that the exponent p is not 4, which would be the case for an isothermal gas cylinder in hydrostatic equilibrium (Ostriker 1964). Palmeirim et al. (2013) introduced a possible explanation for why $p \approx 2$ at large radii, explaining that dense filaments may not be strictly isothermal, but may be better described by a polytropic equation of state, $P \propto \rho^\gamma$ or $T \propto \rho^{\gamma-1}$ with $\gamma \leqslant 1$. Observational measurement of the mean dust temperature profile measured perpendicular to the B213/B211 filament in Taurus shows the best polytropic model fit to temperature is achieved with a polytropic index $\gamma = 0.97 \pm 0.01$ (see Palmeirim et al. 2013, for further details). Dust temperatures in the filament are on the order of 10-15K and this model assumes $T_{gas} = T_{dust}$. However, filaments may be more dynamic systems than the static equilibrium assumed therein.

Arzoumanian et al. (2011) also found that when averaged over the length of the filaments, the diameter $2 \times R_{flat}$ of the flat inner plateau in the radial profiles for 27 filaments in Gould belt clouds is a remarkably constant 0.1 ± 0.03 pc. Arzoumanian et al. conclude there is no correlation between filament width and central column density for the Gould belt clouds. Considering this further, from their figure 7, filament widths range from the half peak beam width (HPBW) resolution limit of 0.03 pc up to 0.1 pc in Polaris, from the HPBW resolution limit of 0.05 pc to 0.2 pc in Aquila and from the HPBW resolution limit of 0.08 pc to 0.2 pc in IC5146. Other authors have found larger values for filament full widths at half-maximum (FWHM). Hennemann et al. (2012) found widths between 0.26 pc and 0.34 pc for the DR21 ridge and filaments in Cygnus X and similarly Juvela et al. (2012) found FWHM of around 0.32 pc for filaments within the *Planck* Galactic cold cores.

Line emission observations of $C^{18}O$ and N_2H^+ and other molecules towards star forming filaments (Zuckerman & Palmer 1974; Arzoumanian et al. 2013; Hacar et al. 2013; Furuya, Kitamura & Sinnaga 2014; Henshaw et al. 2014; Jiménez-Serra et al. 2014; Li et al. 2014) have revealed non-thermal line broadening. Arzoumanian et al. (2013) presented molecular line measurements of the internal velocity dispersions in 46 *Herschel* identified filaments. Noting the thermal sound speed of $\sim 0.2\,\mathrm{km\,s^{-1}}$ for T=10 K, they found velocity dispersions in the range 0.2-0.4 $\mathrm{km\,s^{-1}}$ for thermally subcritical and nearly critical filaments, implying the level of "turbulent" motions is almost constant and does not dominate over thermal support. For thermally supercritical filaments (i.e. they contain more mass than the thermal pressure can withhold), they find a positive correlation between filament column density and the level of turbulent motions, observing velocity dispersions up to $0.6\,\mathrm{km\,s^{-1}}$. This points to an additional source driving these motions, generally regarded as turbulent, the origin of which is unclear. First interpreted as indications of gravitational collapse (Goldre-

ich & Kwan 1974), the scales were rapidly noted to be too small, but several mechanisms have since been proposed as the source, including protostellar outflows, expanding HII regions, stellar winds and internal supernovae (SNe), external SNe, colliding flows or tidal forces and accretion and collapse (see Ibáñez-Mejía et al. 2015, and references therein for a more complete discussion). Observations indicate that the driving source is on the largest scales in molecular clouds (Mac Low & Ossenkopf 2000; Brunt 2003; Brunt, Heyer & Mac Low 2009) making it difficult for internal point sources, e.g. stellar feedback, to drive the large-scale flows. Self-gravity or multiple combined SNe have recently emerged as leading candidates (Ibáñez-Mejía et al. 2015) but the debate is not settled.

Large-scale and well-ordered magnetic fields have been revealed through polarisation measurements towards star-forming filaments. In many cases, the magnetic field appears to be roughly perpendicular to the filaments (e.g. Chapman et al. 2011; Sugitani et al. 2011; Planck Collaboration 2014a). There are some reports though of a bimodal distribution of field directions - either parallel or perpendicular to the major axis of the filament itself (Li et al. 2013; Pillai et al. 2015; Planck Collaboration 2014b). Lower density filaments parallel to the magnetic field have been coined "striations" marking the flow of material along field lines accreting onto the denser perpendicular filaments to which they are connected (Hacar et al. 2013).

Analytical studies have also shed light on the stability and fragmentation properties of filaments subject to turbulent motions, external pressure confinement and accretion on the filament (see, e.g. Ostriker 1964; Inutsuka & Miyama 1992; Fischera & Martin 2012; Pon, Johnstone & Heitsch 2011; Pon et al. 2012; Toalá, Vázquez-Semadini & Gómez 2012; Heitsch 2013). Magnetic fields have generally been found to have a positive effect on filament stability (Nagasawa 1987; Fiege & Pudritz 2000; Heitsch 2013; Tomisaka 2014). Soler et al. (2013) combined numerical simulations of magnetised molecular clouds and synthetic polarisation maps in order to show that the relative orientation of the magnetic field also depends on the initial magnetisation of the filament-forming cloud. This conclusion has been used to infer details of the driving process: super-Alfvénic turbulence causes strong compression, resulting in magnetic fields parallel to the filamentary structures (Padoan et al. 2001), whereas sub-Alfvénic gravitational contraction moves material along the magnetic field lines, generating filamentary structures preferentially perpendicular to the magnetic field (Nakamura & Li 2008).

3 FORMATION MODELS OF FILAMENTS

Theoretical descriptions of filaments have focussed on several different kinds of possible filament states: 1) equilibria, 2) collapsing and fragmenting systems that follow from unstable equilibria, 3) equilibria undergoing considerable radial accretion and 4) highly dynamical systems for which equilibrium descriptions do not apply. We refer the interested reader to a full discussion elsewhere (e.g. see Section 5 of André et al. 2014) and go on to discuss formation mechanisms relevant to our work.

Early simulations have shown that gas is rapidly compressed into a hierarchy of sheets and filaments, without the aid of gravity (Bastien 1983; Porter, Pouquet & Woodward 1994; Vázquez-Semadini 1994; Padoan et al. 2001). Turbulent box simulations and colliding flows (e.g. Mac Low & Klessen 2004; Hennebelle et al. 2008; Federrath et al. 2010; Gómez & Vázquez-Semadini 2014; Moeckel & Burkert 2015; Smith, Glover & Klessen 2014; Kirk et al. 2015) produce filaments. Hennebelle & André (2013) demonstrated the formation of filaments through the velocity shear that is common in magnetised turbulent media. Other authors have explained filaments as the stagnation regions in turbulent media (Padoan et al. 2001). As discussed in the previous section, the formation of filaments preferentially perpendicular to the magnetic field lines is possible in strongly magnetised clouds (Li et al. 2010). André et al. (2014) note that the same 0.1 pc filament width is measured for low-density, subcritical filaments suggesting that this characteristic scale is set by the physical processes producing the filamentary structure. Furthermore, they note that at least in the case of diffuse gravitationally unbound clouds (e.g. Polaris), gravity is unlikely to be involved. Large-scale compression flows, turbulent or otherwise, provide a potential mechanism, but it is not clear why any of these would produce filaments with a constant radius.

Filaments also form due to gravitational instabilites in self-gravitating sheets if the exciting modes are of sufficiently long wavelength (e.g. Nakajima & Hanawa 1996; Umekawa et al. 1999). Layers threaded by magnetic fields still fragment, but the growth of perturbations perpendicular to the magnetic field are suppressed when the thickness of the sheet exceeds the thermal pressure scale height according to the linear analysis of Nagai, Inutsuka & Miyama (1998). The perturbations parallel to the field are unaffected. Therefore filaments perpendicular to the magnetic field form first within the sheet, before they form any cores (Inutsuka & Miyama 1992). Van Loo, Keto & Zhang (2014) showed numerically that filaments with properties similar to the observations indeed form by gravitational instabilities, but that cores form simultaneously.

Recently, (Smith, Glover & Klessen 2014, hereafter SGK14) and (Kirk et al. 2015, hereafter KKPP15) investigated the formation and evolution of filaments in more detail. SGK14 examined the influence of different types of turbulence, keeping the initial mean density constant in simulations without magnetic fields. Specifically they examined three turbulent initial conditions: solenoidal, compressive, and a natural mix of both - two-thirds solenoidal, one-third compressive. All were initialised with the magnitude of the root-mean-square turbulent velocity normalised such that the kinetic and gravitational potential energies are equal at the start of the simulation. They used the moving mesh code AREPO and identified and categorised simulated filaments from column density plots in the same manner as undertaken for recent *Herschel* observations. They found that when fitted with a Plummer-like profile, the simulated filaments are in excellent agreement with observations, with $p \approx 2.2$, without the need for magnetic support. They found an average FWHM of ≈ 0.3 pc, when considering regions up to 1 pc from the filament centre, in agreement with predictions for accreting filaments. Constructing the fit using only the inner regions, as in *Herschel* observations, they found a resulting FWHM of ≈ 0.2 pc.

KKPP15 used the FLASH hydrodynamics code to perform numerical simulations of turbulent cluster-forming regions, varying density and magnetic field. They used HD and MHD simulations, initialised with a supersonic ($M \approx 6$) and super-Alfvénic ($M_A \approx 2$) turbulent velocity field, chosen to match observations, and identified filaments in the resulting column density maps. They found magnetic fields have a strong influence on the filamentary structure, tending to produce wider, less centrally peaked and more slowly evolving filaments than in the hydrodynamic case. They also found the magnetic field is able to suppress the fragmentation of cores, perhaps somewhat surprisingly with super-Alfvénic motion involved in the initial condition. Overall, they noted the filaments formed in their simulations have properties consistent with the observations they set out to reproduce, in terms of radial column density profile, central density and inner flat radius.

Motivated by observed filamentary structure and the need to physically establish such structure within a hydrodynamic context for massive star feedback simulations, this study presents 2D fixed-boundary simulations and 3D free boundary simulations of an approach to the formation of the filaments: specifically, the action of the thermal instability (hereafter the TI) in a stationary quiescent diffuse molecular cloud initially in thermally unstable pressure equilibrium, confined by its low density surroundings, with only 10% density variations seeded across the 100 pc diameter cloud.

Parker (1953) was one of the first to suggest that condensation phenomena in molecular clouds could be a consequence of the instability that is a result of the balance between heating and cooling processes in a diffuse medium. Field (1965) showed that the TI can lead to the rapid growth of density pertubations from infinitesimal density variations, $\delta\rho$, to non-linear amplitudes on a cooling time-scale, which for typical ISM conditions is short compared to the dynamical time-scale. The TI develops an isobaric condensation mode and an acoustic mode, which - under ISM-conditions - is mostly damped. The condensation mode's growth rate is independent of the wave length. However, since it is an isobaric mode, smaller pertubations will grow first (Burkert & Lin 2000). The signature of the TI is fragmentation and clumping as long as the sound crossing time is smaller than the cooling time-scale. Kritsuk & Norman (2002a,b) found that the TI can drive turbulence in an otherwise quiescent medium, even continuously, if an episodic heating source is available.

A number of authors have investigated analytically the effects of different mechanisms on the TI (Birk 2000; Nejad-Asghar & Ghanbari 2003; Stiele, Lesch & Heitsch 2006; Fukue & Kamaya 2007; Shadmehri 2009). Other groups have numerically investigated flow-driven molecular cloud formation including the effects of the TI (e.g. Lim, Falle & Hartquist 2005; Vázquez-Semadini et al. 2007; Hennebelle et al. 2008; Heitsch, Stone & Hartmann 2009; Ostriker, McKee & Leroy 2010; Van Loo, Falle & Hartquist 2010; Inoue & Inutsuka 2012). This numerical work has included magnetic fields, self-gravity and the TI and has identified the thermal and dynamical instabilities that are responsible for the rapid fragmentation of the nascent cloud, largely through flow-driven scenarios. Here we concentrate on the TI itself without any initial flow. As overdense regions appear in the molecular cloud, we continue each simulation with and without self-gravity in order to quantify the effect of gravity on this large-scale initial stage of filament formation. We analyse the properties of these filamentary structures and compare them to the observational properties detailed above.

4 NUMERICAL METHODS AND INITIAL CONDITIONS

4.1 Numerical methods

We present 2D and 3D, magneto-hydrodynamical (MHD) simulations of filament formation from the diffuse atomic medium with and without self-gravity using the established astrophysical code MG (Falle 1991). The code employs an upwind, conservative shock-capturing scheme and is able to employ multiple processors through parallelisation with the message passing interface (MPI) library. MG uses piecewise linear cell interpolation to solve the Eulerian equations of hydrodynamics. The Riemann problem is solved at cell interfaces to obtain the conserved fluxes for the time update. Integration in time proceeds according to a second-order accurate Godunov method (Godunov 1959). A Kurganov Tadmor (Kurganov & Tadmor 2000) Riemann solver is used in this work. Self-gravity is computed using a full-approximation multigrid to solve the Poisson equation.

The adaptive mesh refinement (AMR) method (Falle 2005) employs an unstructured grid approach. By default, the two coarsest levels (G0 and G1) cover the whole computational domain; finer grids need not do so. Refinement or derefinement is based on error. Where there are steep gradients of variable magnitudes such as at filaments, flow boundaries or discontinuities, this automated meshing strategy allows the mesh to be more refined than in more uniform areas. Each level is generated from its predecessor by doubling the number of computational grid cells in each spatial direction. This technique enables the generation of fine grids in regions of high spatial and temporal variation, and conversely, relatively coarse grids where the flow field is numerically smooth. Defragmentation of the AMR grid in hardware memory is performed at every time-step, gaining further speed improvements for negligible cost through reallocation of cells into consecutive memory locations. The simulations presented below employed 7 or 8 levels of AMR. The coarsest level, G0, was set with a very small number of cells in order to make the calculation of self-gravity as efficient as possible, specifically 4×4 ($\times 4$) in 2D (3D). Thus, the highest levels of grid resolution were either G6 with 256×256 ($\times 256$) cells or G7 with 512×512 ($\times 512$) cells. Physical domain sizes and hence physical resolutions varied as detailed below.

4.2 Heating and cooling processes

As the exploration of the evolution of thermal instability in the diffuse atomic medium under the influence of magnetic fields and gravity is the aim of this paper, care has been taken to implement realistic equilibrium heating and cooling, as it is the balance of these processes that is used to initialise the medium in the warm unstable phase and the combined effect of these that defines the evolution of the medium. In the ISM, heating as defined by the coefficient

Γ, varies with increasing density as the starlight, soft X-ray and cosmic ray flux are attenuated by the high column density associated with dense clouds. Because the exact form of the attenuation depends on details which remain uncertain (e.g. the size and abundance of PAHs), the heating rate at T $\leqslant 10^4$ K is similarly uncertain. In this work, as a first step, we have therefore assumed that $\Gamma = 2 \times 10^{-26}$ erg s^{-1} (independent of density or temperature). For the low-temperature cooling ($\leqslant 10^4$ K), we have followed the detailed prescription of Koyama & Inutsuka (2000), fitted by Koyama & Inutsuka (2002), corrected according to Vázquez-Semadini et al. (2007), namely

$$\frac{\Lambda(T)}{\Gamma} = 10^7 \exp\left(\frac{-1.184 \times 10^5}{T + 1000}\right) + 1.4 \times 10^{-2}\sqrt{T}\exp\left(\frac{-92}{T}\right). \quad (3)$$

The resulting thermal equilibrium pressure P_{eq} and thermal equilibrium temperature T_{eq}, defined by the condition $\rho^2\Lambda = \rho\Gamma$, are shown in Fig 1(a) as a function of density. Given the above forms of heating and cooling, it is possible to scale non-gravitational simulations under the following transformation $\rho \rightarrow \alpha\rho$, $\Gamma \rightarrow \alpha\Gamma$, $t \rightarrow t/\alpha$, $l \rightarrow l/\alpha$ where α is constant. This allows one to model different regions of the Galaxy which have different heating rates (see e.g. Wolfire et al. 1995, 2003).

At temperatures above 10^4 K we have followed the prescription of Gnat & Ferland (2012) who used CLOUDY 10.00, enabling us to define cooling rates over the temperature range from 10 K to 10^8 K. This has been implemented into MG as a lookup table for efficient computation. We do not expect such high temperatures in these simulations, but in order to enable stars and their associated wind and SNe feedback to be introduced into these simulations in future, a consistent approach from the outset has been used.

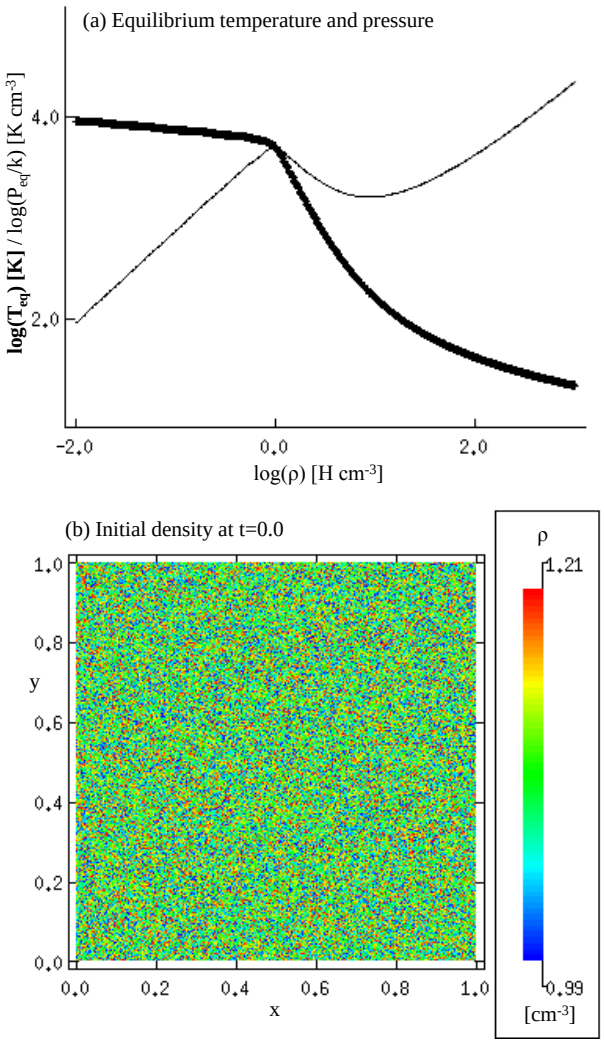

Figure 1. (a) Thermal equilibrium pressure (P_{eq}/k - thin line) and temperature (T_{eq} - thick line) vs. density for the cooling and heating functions given in Section 4.2 and used to set the pressure and temperature in the initial condition. (b) The initial density distribution across a 2D domain, showing 10% density variations. Length is scaled in units of 50 pc.

4.3 Initial conditions

The physical properties of our initial condition are motivated by the simplification of initial conditions and the need to avoid physical (or numerical) conditions which may preset a length scale in the simulation. For example, KKPP15 found that the injection of velocity on a particular forcing scale, as often used to initialise turbulent ISM conditions, can strongly affect the mean separation of filaments formed in the hydrodynamic case and to a lesser extent the magnetised case. We also take care to avoid numerical issues, e.g. instability-smoothing caused by AMR derefinement, as discussed further below. In this way, we can examine the effect of the thermal instability on diffuse medium evolution in isolation.

In our initial condition we set a number density of atomic hydrogen throughout the medium of $n_H = 1.1$ cm^{-3}. Following Field (1965), we seed the domain only with random density variations - 10% about this uniform initial density. We show the density distribution in Figure 1(b). Care is taken to avoid repeating random number generation in multi-processor execution, by spooling through the random number sequence independently according to processor number on each processor. This initial density is at the lower end of the range of thermally unstable densities for the balance of heating and cooling functions used in this work, approximately n_H = 1–7 cm^{-3} defined by the region of negative gradient in the function of thermal pressure according to density shown in Figure 1(a). Tests with a number of initial densities and ± 0.1 cm^{-3} variations across this range showed that a lower density triggers the formation of higher density structures on shorter timescales. Thus, the low value of initial density that we selected ensures that structure forms on the shortest timescales. From an evolutionary point of view, it would seem likely that mechanisms that form clouds from the ISM are likely to increase the density from typical ISM densities of 1 H cm^{-3} or less into the lower end of the unstable phase first, although the passage of a shock may also jump the density straight to the upper end of the unstable regime, or higher, and several authors have investigated this as previously noted. For the purposes of this investigation, we choose the former evolutionary process and consider the initial density that most quickly forms higher density struc-

tures whilst remaining on the equilibrium curve. Initial pressure is set according to the unstable equilibrium of heating and cooling at $P_{eq}/k = 4700 \pm 300$ K cm^{-3} and results in an initial temperature $T_{eq} = 4300 \pm 700$ K. The dependence of the equilibrium pressure on the density of the medium is shown by the thin line in Figure 1(a). Equilibrium temperatures are indicated by the thick line in Figure 1(a). The material is stationary.

In all cases, we follow the evolution for approximately a free-fall time of a diffuse medium at this density, where free-fall time t_{ff} is defined as

$$t_{ff} = \sqrt{\frac{3\pi}{32G\rho}} \quad (4)$$

and for these initial densities, $t_{ff} = 49.1$ Myrs.

For this work, we thread the domain with uniform B-field along the x direction, i.e. $\mathbf{B} = B_0\ \hat{\mathbf{I}}_x$. We investigate three magnitudes of the magnetic field, defined by a plasma $\beta = \infty$, 1.0 and 0.1. In the case of $\beta = \infty$, there is no magnetic field ($B_0 = 0$). In the moderate field case of $\beta = 1.0$, there is pressure equality, i.e. the thermal pressure at $n_H = 1.1$ cm^{-3} is equal to the magnetic pressure at $t = 0$, and $B_0 = 1.15\,\mu$G. In the strong field case of $\beta = 0.1$, the magnetic pressure is $10\times$ greater than the thermal pressure at $t = 0$. The magnetic field strength is increased by a factor of $\sqrt{10}$ to $B_0 = 3.63\,\mu$G. Both cases represent field strengths similar to mean Galactic values expected at an inner (~ 4 kpc) location and would be representative of the magnetic field conditions in which diffuse clouds begin to condense and form higher density structures. Evolved molecular clouds have been noted to have magnetic field strengths over $10\times$ greater than these, but it is not clear how these field strengths have been generated. In this work, we examine whether thermal instability leading to filament formation under the influence of gravity alone can intensify the magnetic field, or whether other influences are required, for example stellar feedback generating super-sonic, super-Alfvénic motions.

We considered three separate Scenarios, employing 2D XY and 3D XYZ Cartesian grids, in order to examine the evolution of the thermal instability:

4.3.1 Scenario 1 - a segment of a larger cloud (2D)

In this Scenario, 2D simulations employed fixed boundary conditions that enforced the initial condition at all boundaries in order to represent a segment of a larger molecular cloud. Periodic boundary conditions were avoided in order to allow the use of self-gravity. Three simulations were performed without self-gravity for the three magnetic field cases $\beta = \infty$, 1.0 and 0.1, and then repeated with self-gravity. In every simulation, the domain was filled with the initial condition detailed above, as shown in Figure 1(a). The physical domain size was 50 pc^2 throughout, with G0 containing 20×20 cells and 5 or 6 levels of AMR initially, resulting in a resolution 0.15625 pc on G4 or 0.078125 pc on G5 (640×640). In all these simulations, the AMR capability was disabled and 5 or 6 complete grid levels were simulated as tests showed that during the initial evolution of the medium, the density variations seeded in the initial condition initially smoothed out before condensations appeared across the cloud. Hence the AMR grid would by default completely derefine, suppressing condensations. Further tests, not shown, were also carried out with both half-physical-size domains and double resolution domains, hence twice the physical resolution on the finest grid level. These tests converged with the lower physical resolution simulations, in terms of the numbers of structures, their size and separation.

4.3.2 Scenario 2 - a slice of an infinite cylinder (2D)

In this Scenario, a circular stationary diffuse cloud of radius 50 pc was placed at the origin (0,0) in a domain of physical extent ± 75 pc in both directions (150 pc square), surrounded by a lower density stationary medium. The minimum 25 pc buffer around the cloud in all directions avoided any boundary-related numerical effects. Free-flow boundary conditions were employed on all boundaries. Again, three simulations were performed without self-gravity for the three magnetic field cases, and then repeated with self-gravity. The same initial condition as previously noted was adopted inside the cloud and the cloud was assumed to have a definite edge, i.e. no smoothing between the cloud and its surroundings was adopted. The surrounding medium was set with a density of 0.1 H cm^{-3} in pressure equilibrium with the cloud and hence at a high temperature. If allowed to evolve this surrounding medium would cool rapidly. As we are not interested in the evolution of the surrounding medium and its pressure is simply defined in order to confine the cloud but not affect its internal evolution, heating and cooling was disabled in the surrounding medium. The same effect was achieved in Scenario 1 by the use of fixed boundary conditions.

4.3.3 Scenario 3 - a spherical cloud (3D)

In this Scenario, the same stationary diffuse cloud of radius 50 pc was surrounded by a stationary medium in a 150 pc cube 3D domain. The same initial conditions as previously were adopted, both inside the cloud, resulting in a total cloud mass of $\sim 17,000\,M_\odot$, and also in the surrounding medium outside the cloud. In this Scenario, G0 contained $4 \times 4 \times 4$ cells and the simulation employed 8 levels of AMR, equivalent to a $512 \times 512 \times 512$ grid and a finest resolution of 0.29 pc on a side. A low resolution G0 was adopted in order to make the calculation of self-gravity more efficient. Levels G0 to G5 were initially complete in order to avoid the numerical AMR instability-smoothing issues discussed above. Levels G6 and G7 were allowed to refine or derefine according to the physical conditions in the domain. Tests again showed that this approach and resolution captured the true physical evolution of the cloud and avoided coarse grid scales affecting the formation and evolution of higher density structures. No symmetry constraints were imposed on the simulation and all quadrants were calculated so that asymmetric structure can develop freely throughout the cloud. Free-flow boundary conditions were used at all boundaries.

4.4 Neglected processes and simplifications

This work is the first step in developing realistic molecular cloud conditions for stellar feedback simulations, such as we have performed previously with predefined cloud conditions

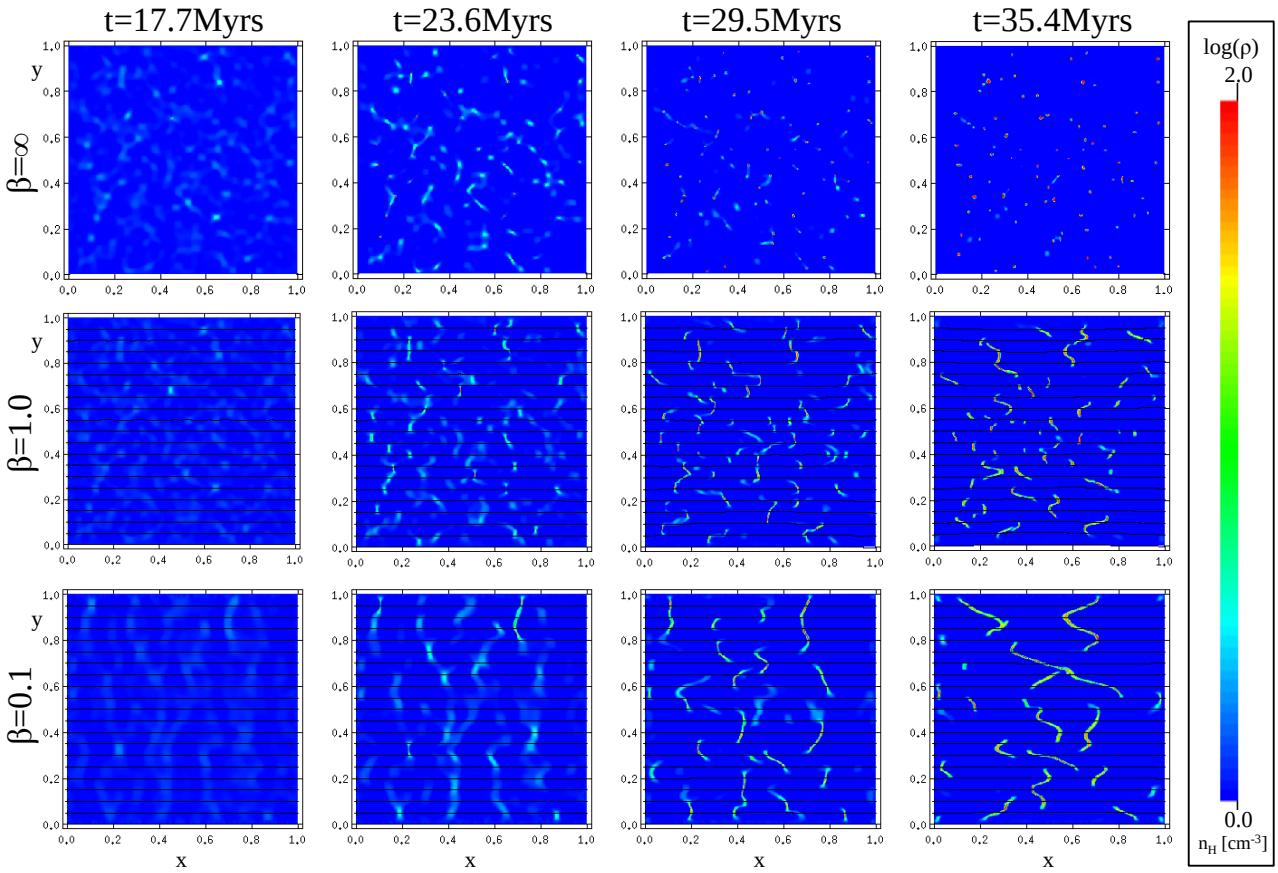

Figure 2. Scenario 1 - 2D simulations of segments of a larger cloud, *without* self-gravity. Each plot shows the logarithmic mass density. Across the rows, the three different magnetic field cases are presented. Magnetic field lines are indicated where appropriate. Length is scaled in units of 50 pc.

(Rogers & Pittard 2013, 2014). We have accounted for radiative heating and cooling, gravity and magnetic fields. We have necessarily still made a number of simplifications and approximations.

We model equilibrium cooling only and neglect the role of molecular cooling, including carbon monoxide (CO). Without a full treatment of heating according to column density and shielding to allow the formation of CO, it is difficult to justify the inclusion of any CO effects into the cooling curve. That said, we have performed a small number of tests with just such an amendment to the low temperature cooling, as used by Rogers & Pittard (2013, 2014). We have found that the increased cooling introduced by CO at lower temperature allows the clumps and filaments to cool further (with associated increased density) to temperatures on the order of 10-15 K. With regard to this work, it should be noted that the densities we find are likely to be at the lower end of the range of observed clump and filament densities. We leave a more complete treatment of the role of CO to a future work. Internal photoionisation does not play a role as no stars have formed yet in these molecular clouds. In a forthcoming work, we examine the introduction of stars and their wind and SNe feedback into the cloud.

5 RESULTS

In this section we present our results. Firstly, we examine the evolution of the Scenario 1 2D box simulations (Section 5.1). Next we focus upon the evolution of the 2D diffuse cloud simulations up to a free-fall time in Section 5.2. Finally, in Section 5.3 we present the evolution of the 3D diffuse cloud simulations, presenting slices through the simulation domain parallel and perpendicular to the imposed field, as well as collapsing the simulation domain perpendicular to the imposed field. In the following Section 6 we analyse and discuss the properties of the individual clumps and filaments.

In the following sub-sections, we refer to the formation of clumps from the diffuse cloud. We separate the terminology in this fashion to achieve clarity for the reader, although it should be noted that our definitions do not track identically with those typical of other authors, e.g. Table 1 of Bergin & Tafalla (2007). Our "clumps" are similar to Bergin & Tafalla's clouds, although our velocity dispersions are lower, for reasons investigated in the next Section.

5.1 Scenario 1 - a segment of a larger diffuse cloud

We begin by showing the time evolution of the three *diffuse cloud segment* simulations without self-gravity in Scenario 1

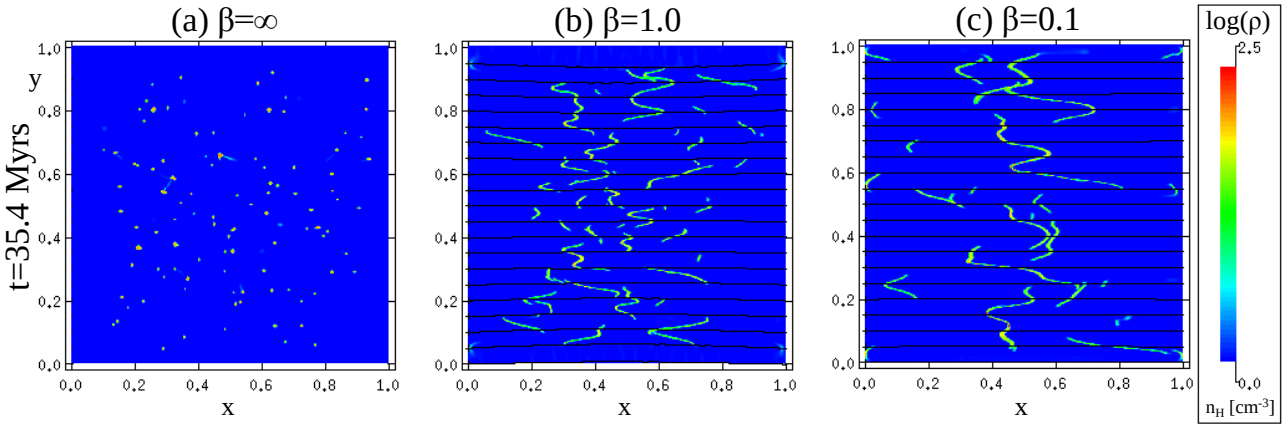

Figure 3. Scenario 1 - 2D simulations of segments of a larger diffuse cloud, *with* self-gravity. Each plot shows the logarithmic mass density. Across the columns, the three different magnetic field cases are presented, all at the same snapshot time in the simulation of 35.4 Myrs. Magnetic field lines are indicated where appropriate. Length is scaled in units of 50 pc.

(Fig. 2). In the first 10 Myrs, all cases evolve to smooth the initial density pertubations shown in Fig. 1(a). Material in isolated unstable thermal equilibrium can then evolve into one of two stable states – either it contracts and cools into the cold state, or warms and expands into the warm state. We observe regions of the domain undergoing precisely this – some begin to cool and contract to higher density, others begin to warm and reduce in density. The flow of material from warm to cool regions then accentuates the density inhomogeneities further. In the absence of magnetic field and gravity, the distribution and growth rates of the high density regions is controlled by the TI ($\beta = \infty$, top row Fig. 2). The initial smoothing has no preferred direction and condensations appear after 18 Myrs with densities a few tens of times higher than the initial condition across the domain. By 24 Myrs, it's clear that these "clumps" are not growing at the same rate; some are already far denser than others. Mass flows onto the clumps from all directions equally and hence the clumps are randomly distributed across the domain. Lower density linear structures interconnect a number of the clumps. These structures fit the definition of filaments, but are in fact transitory structures of material flowing towards higher density clumps. An examination of the velocities in the domain confirms this - the clumps are stationary, with material moving onto them equally from all directions, including motion toward clumps along the filamentary structures. The spacing of the clumps is approximately 5-10 pc. By 29.5 Myrs (third column), the number of such linear structures has greatly reduced, although some do persist to 35 Myrs and beyond. The clumps have a range of densities from a few hundred H cm^{-3} up to 1000 H cm^{-3} and are distributed evenly across the domain. The TI has enabled the initial density inhomogeneities to contract into high density clumps on a time-scale considerably shorter than the dynamical free-fall time of the cloud, according to the growth described by Field (1965). The lowest temperatures correspond to the equilibrium conditions observed in the highest density regions, around 30 K. We discuss the properties of the clumps, including temperature and velocity profiles in more detail in Section 6.

The TI generates motions that are sub-sonic outside the cool dense structures and sub-Alfvénic everywhere in the domain. They are on the order of 5 km s^{-1} towards the filaments. The internal motions inside the filaments are also sub-sonic on the order of 0.5 - 0.6 km s^{-1}. In the transition regions, where material reaches the filament, trans-sonic motions are briefly observed. With $\beta = 1.0$ (Fig. 2, second row), the magnetic field preordains the direction for the flow of material - along the field lines only with this velocity range (indicated by lines across the domain). Condensations that have appeared by 18 Myrs show only minor differences to those formed with $\beta = \infty$ at that time. By 23.6 Myrs the linear structures seen previously are now stationary filaments that grow in density at the same rate as the clumps did previously, gaining material from flow along the field lines. By 29.5 Myrs, their nature as persistent and stationary filamentary structures is clear. The highest density filaments are predominantly perpendicular to the magnetic field direction. A number of lower density linear structures 'feeding' the high density filaments are now apparent, which are more likely to be parallel to the field direction, in agreement with the direction of sub-sonic, sub-Alfvénic motion defined by the magnetic field. There are also a number of objects that are more clump-like. They are somewhat extended perpendicular to the field but not enough to be defined as a filament (according to our definition, see Section 2). Both the filaments and the clumps show a similar range of densities, up to a few hundred H cm^{-3} – lower than $\beta = \infty$. Another difference from $\beta = \infty$ is that between 29.5 Myrs and 35.4 Myrs, the filaments now move considerably more, still along the field lines, connecting and forming longer, more curled filaments that have similar densities and widths, but are now considerably longer. Many of the clumps seen at 29.5 Myrs have now been absorbed into these filamentary structures.

With $\beta = 0.1$ (Fig. 2, third row), the magnetic field now dominates the evolution and the only structures that form are filamentary. Rather than growing in length at late times, these filaments initially cool and condense out of the smoothed initial condition as long, high-density structures with high aspect ratios. For the first 30 Myrs, they are almost exclusively perpendicular to the magnetic field. In the final plot (fourth column), after 35.4 Myrs of evolution, the filaments are now skewed across the domain, a consequence

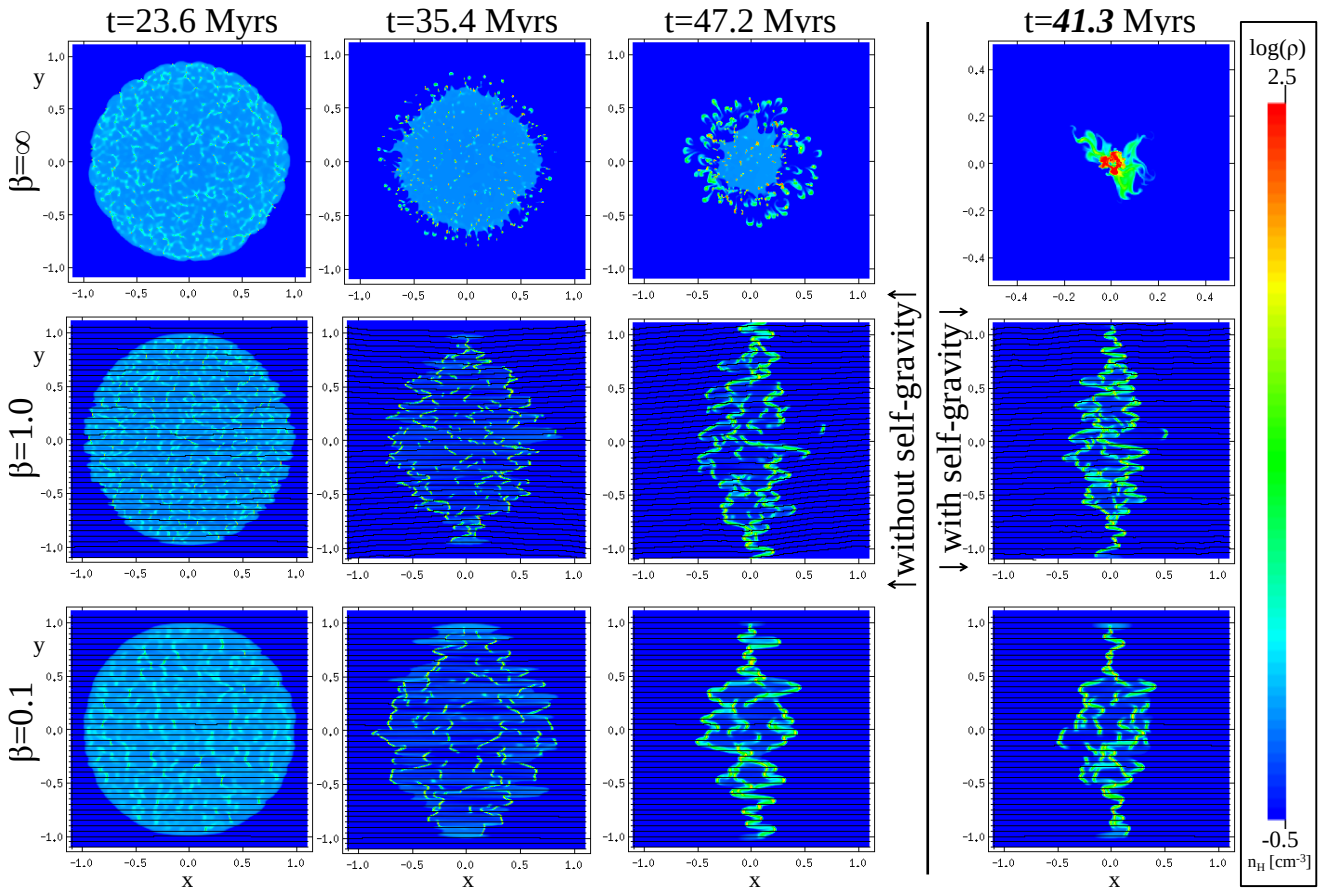

Figure 4. Scenario 2 - 2D simulations of slices perpendicular to the major axis of a larger cylindrical cloud, in columns 1-3 without self-gravity and in column 4 with self-gravity. Each plot shows the logarithmic mass density. Across columns 1-3, time evolution of the simulations without gravity is presented. Across the rows, the three different magnetic field cases are presented. Magnetic field lines are indicated where appropriate. Length is scaled in units of 50 pc.

of the initial random density distribution. The magnetic field remains unaffected by this motion.

In all three cases after 35.4 Myrs, large-scale movement occurs across the entire domain. The effect of self-gravity on this movement is important and so we go on to consider the repeat of these simulations with self-gravity, as shown in Fig. 3. With $\beta = \infty$, the major difference is in the range of clump densities formed during the evolution. Higher density clumps than previously are formed on the same time-scale. In both $\beta = 1.0$ and $\beta = 0.1$ cases, the major difference as expected is at late-time (t=35.4 Myrs $\approx 0.7\,t_{ff}$). Gravitational attraction has resulted in the movement of the filaments towards one another and the centre of the domain, albeit with velocities that are still sub-sonic and sub-Alfvénic and hence the filaments appear to crowd around $x = 0.5$.

We have included this Scenario in order to study and document the action of the TI in isolation, but it is questionable how representative these simulations are of a cloud segment after 30 Myrs. In the next two sections, we model a cloud and surroundings in order to address this point more fully.

5.2 Scenario 2 - slices of cylindrical clouds

In Fig. 4 we show the time evolution of the three magnetic field cases with and without the effect of self-gravity for Scenario 2, representing a slice through a cylindrical cloud perpendicular to the major axis. With $\beta = \infty$, the cloud evolves without any magnetic field and the natural action of the TI can be observed. By 23.6 Myrs, cold condensations have formed across the cloud. As the domain is now considerably larger (shown in the figure is 100 pc×100 pc), many more condensations are apparent in the domain. As before, they evolve to form small, cold, high density clumps by 35.4 Myrs. Motion caused by the TI has caused the contraction due to the pressure loss within the cloud. Self-gravity does not play a role in this simulation. with by late-time (47.2 Myrs), a smaller number of more dense clumps are now apparent, as well as clumps on the outer edge of the cloud losing mass towards the centre of the cloud. Further detailed investigation of the simulation, in particular the velocity in and around the clumps, reveals that they are falling radially inwards at a lower speed than their lower density surroundings. In the frame of reference of the clump, lower density material is therefore flowing past the clump and entraining clump material into the faster flow. The result is the formation of tails behind the clumps and directed radially inwards, as seen in

the figure. Given that around the edges of the cloud, the TI will generate motion toward the centre of the cloud accentuated by the 2D numerical approach, the authenticity of this collapse will be studied in more detail in the next sub-section, considering a 3D simulation.

With the introduction of self-gravity to the $\beta = \infty$ field case, the cloud contracts under the effect of both the TI and gravity to a high density core by 41.3 Myrs, consistent with the free-fall time of 49.2 Myrs. Approximately 17,000 $M_\odot$ is now contained within a radius of 5 pc. Structures formed by the TI during the preceding evolution have been destroyed by the gravitational collapse of the cloud.

With $\beta = 1.0$, structures form across the cloud in the first 25 Myrs in a similar manner to those observed in the $\beta = \infty$ field case. The two clouds are almost indistinguishable. After 25 Myrs, the evolution of these two clouds diverges. With magnetic pressure equal to thermal pressure, filaments and clumps again form across the cloud. The radial contraction of the cloud seen without magnetic field now manifests itself as contraction along the field lines only. An elliptical cloud forms, supported in the direction perpendicular to the magnetic field by the magnetic pressure. The cloud evolves towards becoming a bundle of filaments. By 47.2 Myrs, many of the smaller filaments have now interconnected and formed longer, more curled structures. These have also absorbed many of the clumps that had evolved up to this point. Large-scale motion is directed towards the vertical axis of the cloud, with larger velocities at late-time. In this simulation with self-gravity (as seen in the 4th column of Fig 4), the filaments survive the gravitational collapse. The filaments eventually gather towards the centre of the cloud, moving along the field lines, with the magnetic field providing support against both the TI and the gravitational collapse of the cloud.

In the simulation with $\beta = 0.1$, the effect of a strong magnetic field can be seen even at comparatively early time in the evolution of the cloud. The condensations forming out of the low density cloud are already perpendicular to the field, indicating motion of material is very strongly confined along field lines. By 35.4 Myrs the cloud is dominated by filaments predominantly perpendicular to the imposed field. The TI-driven collapse along the field lines leads more rapidly towards the ordered extended filament situation seen in the $\beta = 1.0$ case, with sub-filaments that contain distinct substructures in both density and velocity. With gravity, the collapse is even more rapid towards this conclusion.

5.3 Scenario 3 - a spherical cloud

We now consider our 3D simulations of spherical clouds. In Fig 5, we show slices through the domain parallel and perpendicular to the magnetic field, as well as projected column densities in order to gain the most insight into the evolution of these molecular clouds. Figures in the previous two Scenarios have shown how the clouds evolve to form filaments, and so in this section we choose to show the cloud at a particular instance in its evolution – 35.4 Myrs – once structure has formed but less than t_{ff}. The evolution up to this point has been illustrated in the previous two Scenarios. Where there are deviations from this evolution, we note those in our description.

With $\beta = \infty$ (Fig. 5, top row), the TI triggers the now familiar formation of cold, dense clumps across the molecular cloud, predominantly towards the edge of the cloud, the properties of which we will discuss in detail in the next section. Planes through the simulation domain at $x = 0$ and $y = 0$ are qualitatively the same in terms of the major characteristics, e.g. overall cloud dimensions, clump distribution, clump density and interclump conditions. The quantitative differences are a consequence of the random initial conditions. Collapse of the datacube along either the z or x axis also results in indistinguishable column density projections. It is worth noting that the spread of clumps across the cloud in projected column density is roughly even, i.e. there is no increased population density towards the centre of the cloud. This indicates the clump formation, at least in this Scenario without self-gravity, is predominantly around the edges of the cloud rather than uniformly across the cloud, which would result in increased clump population density towards the centre of the cloud. Simulated in 3D, it would appear that collapse of the cloud under the influence of the TI alone is less pronounced. Given that in 2D this is caused by velocities developing radially inwards toward the centre of the cloud, in 3D a wider range of directions of velocity can develop and the rapid collapse observed in 2D is revealed as an artifact of 2D modelling. Whilst there are no indications of clump ablation in this simulation at this time, we find similar but less pronounced effects around the edge of the cloud by t_{ff}, ∼53 Myrs.

With a magnetic field with $\beta = 1.0$ (Fig. 5, second row), multiple filaments appear to form uniformly across the cloud, perpendicular to the field direction on both a plane at $y = 0$ and in projection collapsing the density distribution along the z axis. These filaments persist rather than merge. The question of whether these filaments are actually individual filaments or corrugated interconnecting sheets seen in projection can now be addressed. Inspection of the 3D simulation would indicate that for this field strength, without self-gravity, filaments form separately and eventually merge as more material moves out of the thermally unstable state, creating first filaments, then interconnected 'corrugated' sheets, with density varying across the sheet creating structure in the sheet and in projection. A line of sight across the sheet would see several filaments, that are in fact interconnected (see the illustrative line of sight in Fig. 6 for the $\beta = 0.1$ case on the $x = 0$ plane.) The preceding filaments persist for a relatively long period of the evolution - from 25 Myrs to 35 Myrs as noted previously.

Projecting perpendicular to the magnetic field to create a collapsed plane parallel to the field (third column), the cloud appears entirely filamentary. Column densities in the filaments are on the order 10^{-3} – 10^{-2} g cm^{-2}. This is in excellent agreement with range of column densities derived from *Herschel* data in a portion of the Polaris flare translucent cloud André et al. (2010) and also central column densities in the B213/B211 filament in Taurus Palmeirim et al. (2013). The nature of the velocity dispersions in these filaments generated by the TI is on the order of 0.5 - 1.0 km s^{-1}. The velocity variation across the corrugated sheets shows dispersions around separate velocity components for different filaments. Separated velocity components have previously been interpreted as evidence for separated filamentary structures, rather than corrugated sheets. However, it is now clear that corrugated sheets, with velocity variations across

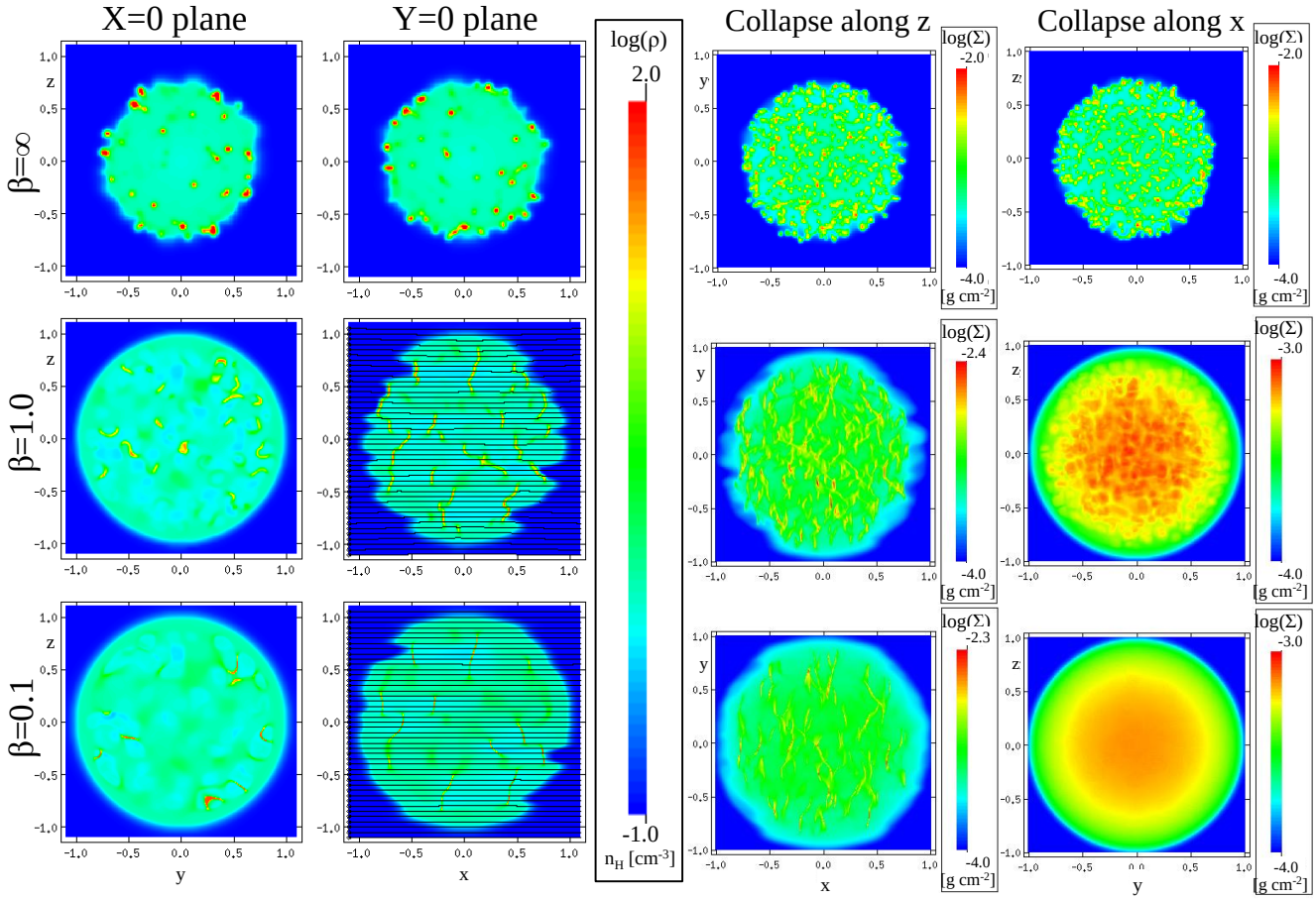

Figure 5. 3D simulations *without* self-gravity at t=35.4 Myrs. Columns 1 and 2 show the logarithmic mass density on planar slices through the domain at $x = 0.0$ perpendicular to the field and $y = 0.0$ parallel to the field respectively. Columns 3 and 4 show the logarithmic column density by projection along the x axis onto a y-z plane and along the z axis onto a x-y plane respectively. Across the rows, the three different magnetic field cases are presented. Magnetic field lines are indicated where appropriate. Length is scaled in units of 50 pc.

the sheets of several km s^{-1} (up to 10× larger than the non-thermal velocity dispersions) and density variations caused by the TI leading to a filamentary appearance in projection, can also generate separated velocity components, with dispersion around these components. This indicates that separated velocity components should not be used to differentiate between filamentary structures and corrugated sheets seen in projection.

The major axis of the filamentary structures are perpendicular to the magnetic field, although corrugations in the sheets show structures which are parallel to the field in places. Unlike in the previous Scenario (c.f. Fig 3), there are no indications of isolated clumps in this cloud. As in the previous Scenario, the highest density filaments are exclusively perpendicular to the magnetic field. The lower density filamentary structures interconnecting these high-density filaments are again regions still undergoing TI-driven condensation flowing onto the higher-density filaments. Projecting along the magnetic field to create a collapsed plane perpendicular to the field (fourth column), shows structure apparent in the cloud, but it is not clear that it is at all filamentary. A cloud seen along a line of sight perpendicular to the field (third column) can appear very different from the same cloud seen along a line of sight parallel to the field (fourth column).

With $\beta = 0.1$ (Fig. 5, third row), fewer filaments form and they are exclusively perpendicular to the magnetic field. The average filament spacing would appear to be larger than in the $\beta = 1.0$ case. Seen in projected column density, the cloud appears filamentary when the line of sight is perpendicular to the field and *uniform* when the line of sight is parallel to the field. Comparable column densities to the $\beta = 1.0$ case and observations are produced perpendicular to the field. Parallel to the field, column densities are 10× lower. Clearly β is low enough to enforce no movement of material across field lines – due to entirely sub-Alfvénic velocities. We are not aware that such strongly contrasting numerical outcomes have been seen before when considering projected column densities. KKPP15 shows filaments appear filamentary when projected in all three directions, although they only show column density distribution projected along the x axis in their simulations.

In Fig. 6 we show the evolution of the spherical cloud including the effect of self-gravity. Without a magnetic field, the cloud undergoes gravitational collapse and shrinks as shown in the top row of Fig. 6. Unexpectedly, the projected

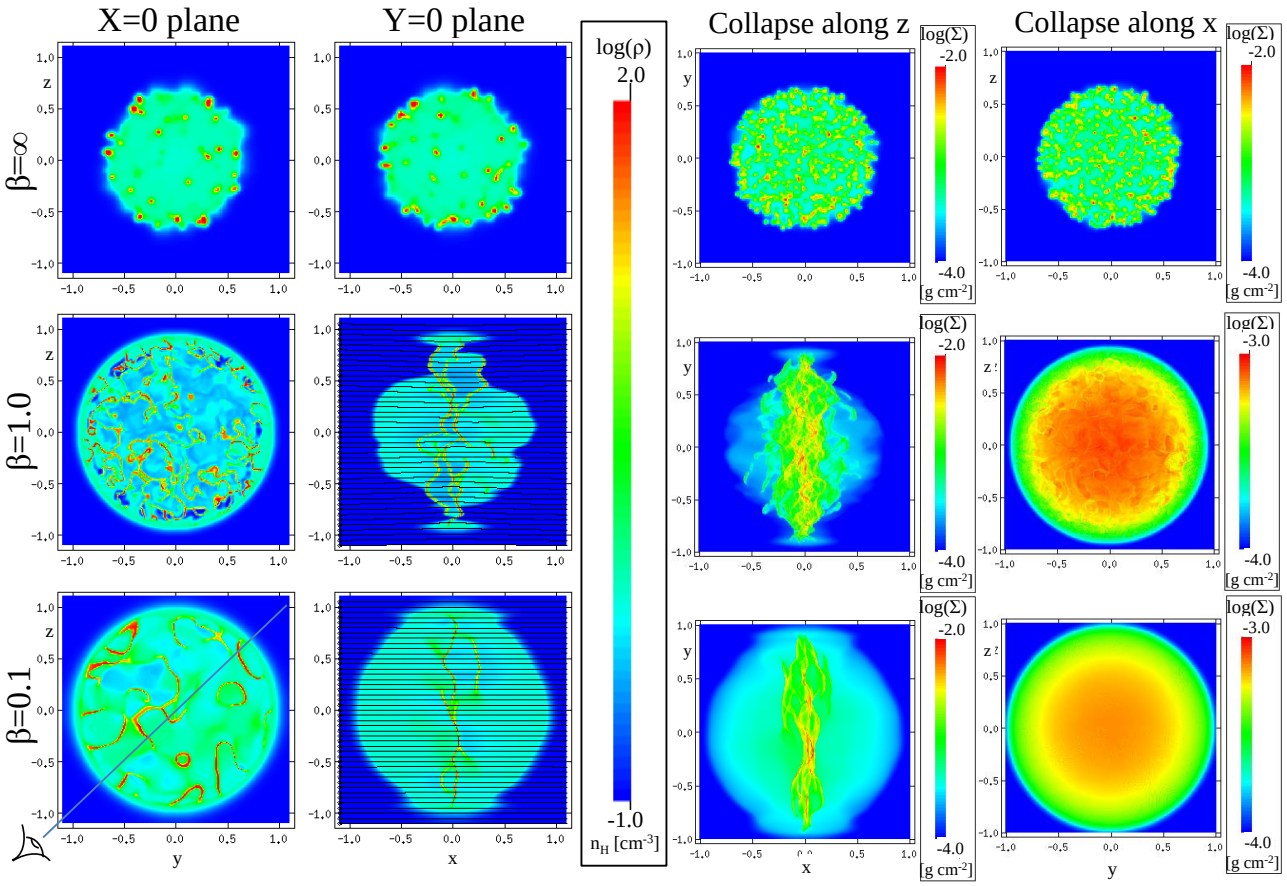

Figure 6. 3D simulations *with* self-gravity at t=35.4 Myrs. Columns 1 and 2 show the logarithmic mass density on planar slices through the domain at $x = 0.0$ perpendicular to the field and $y = 0.0$ parallel to the field respectively. Columns 3 and 4 show the logarithmic column density by projection along the x axis onto a y-z plane and along the z axis onto a x-y plane respectively. Across the rows, the three different magnetic field cases are presented. Magnetic field lines are indicated where appropriate. Length is scaled in units of 50 pc.

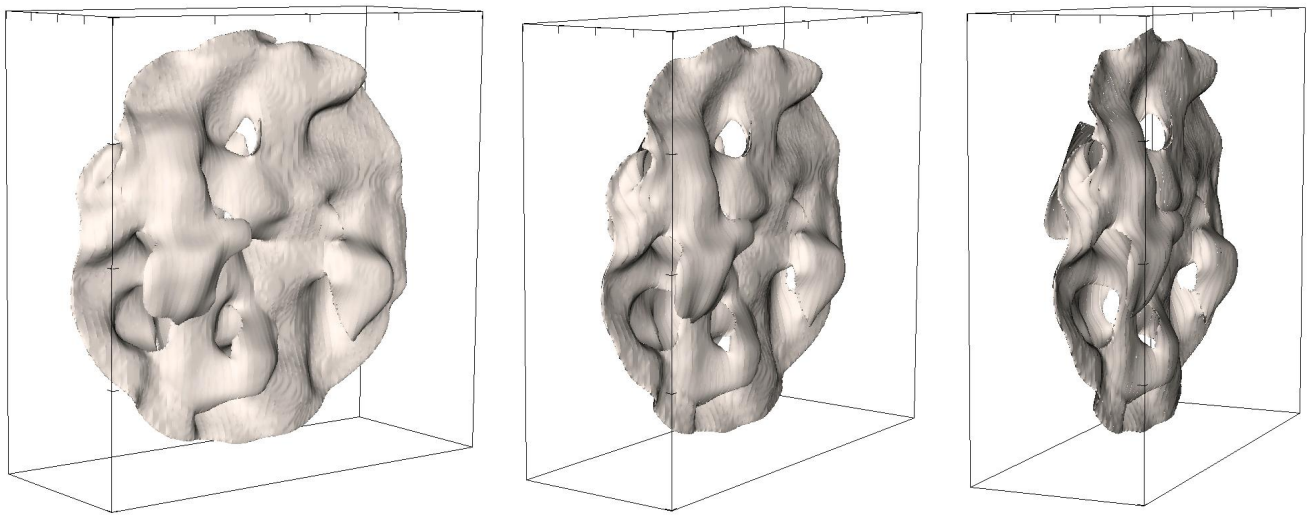

Figure 7. Three different views of the same 3D isosurface of constant density (10 cm^{-3}) illustrating the corrugated nature of the single sheet formed in the $\beta = 0.1$ case with self-gravity at 35.4 Myrs. Visualisation created using the VisIt software (VisIt Collaboration 2012). Length is scaled in units of 50 pc.

column density both along x and z reveals a few linear filamentary structures connecting the high density clumps. Although there are some linear structures visible in the $y = 0$ plane, it is more than likely that these are in fact a projection effect. With $\beta = 1.0$ (Fig. 6, second row), filaments that initially formed all across the cloud in the simulation without gravity, have now formed predominantly around x=0 and are merging to form a complex bundle of filaments seen in projection across the field (third column). In reality, this is the projection of a number of interconnecting sheets located roughly parallel to a plane at x=0, rather than individual filaments. Across the field lines, the magnetic field has supported the cloud from TI-driven and gravitational collapse. In the $\beta = 0.1$ case (Fig. 6, third row), by 35.4 Myrs the cloud has formed a single sheet down the centre of the cloud. The slice plane at $x = 0$ (Column 1) highlights the corrugated nature of the sheet. This sheet is notably less corrugated than in the $\beta = 1.0$ case - there are fewer intersections of the sheets shown by the red high density on the x=0 plane. Parallel to the field, the slice plane at $y = 0$ highlights the single filamentary nature of this cloud. 3D isosurfaces of constant density best illustrate the corrugated nature of this sheet, as shown in Fig. 7. Both β=1.0 and 0.1 simulations with self-gravity are more filamentary than in the simulations without self-gravity (c.f. Fig 5). Collapsing along the z-axis to examine the column density, a tightly bound bundle of filaments is the apparent manifestation of the corrugated sheet formed by the thermal instability. Peak column densities are comparable to previously. In projection along the field direction, the same uniform cloud is observed as in the simulation without self-gravity, with no internal structure, but column densities 10× lower. The dominance of the magnetic field has guaranteed that material has only moved along the field lines, resulting in the smooth projection of an apparently uniform density sphere onto this plane. We go on now to examine whether the apparently filamentary structures formed in Scenario 3 with self-gravity in particular show any resemblance to observed structure.

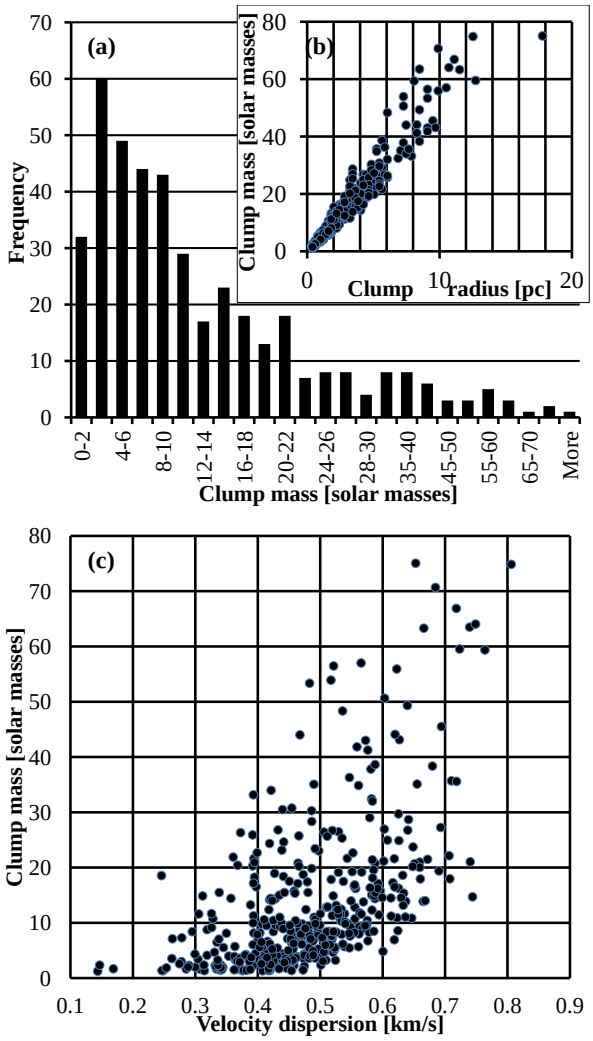

Figure 8. Clump properties from the non-magnetic simulation. (a) mass distribution of 430 clumps. (b) clump mass vs. clump radius. (c) clump mass vs. velocity dispersion inside the clump.

6 CLUMP AND FILAMENT ANALYSIS

6.1 Clumps

Clumps are formed throughout the cloud in all three Scenarios with the $\beta = \infty$ field case and also along with filaments in the $\beta = 1.0$ field case. In this section, we present their properties. We remind the reader that we use "clump" by choice in order to achieve clarity from the diffuse "cloud" initial condition and it should be noted that this definition does not track identically with those typical of other authors, e.g. Table 1 of Bergin & Tafalla (2007).

We have used an algorithm developed for MG (Van Loo, Tan & Falle 2015) in order to identify high density clumps in the 3D $\beta = \infty$ field case with self-gravity. Setting a density threshold of 100 H cm^{-3}, this algorithm scans through the computational domain and firstly identifies all the cells that have a density above this threshold and then within that selection identifies cells that neighbour each other to identify each clump as a whole. We have discounted clumps containing only 1 grid cell from this data analysis. The algorithm identified ∼430 clumps (not including a further 40 single cells with densities above the threshold value). In Fig 8(a) we show the clump mass distribution of these ∼430 clumps. Nearly half of the clumps have a mass less than 10 M$_\odot$. The distribution has a defined peak in the 2-4 M$_\odot$ bin and a long tail, typical of a log-normal distribution, with three clumps with masses greater than 70 M$_\odot$.

In Fig 8(b) we show the distribution of clump mass vs. radius. There is a strong agreement between clump mass M_c and clump radius R_c whereby $M_c \sim 6 \pm 1.5\, R_c$ M$_\odot$. The clump radius ranges up to ∼18 pc, although the next most massive clump has a radius of just over 12 pc *and equivalent mass*; the three most massive clumps range widely in radius from 10 to 18 pc. The average density across all the clumps is 4.9 M$_\odot$ pc^{-3}, with a standard deviation of 0.96 M$_\odot$ pc^{-3}, a maximum value of 8.35 M$_\odot$ pc^{-3} and a minimum value of 3.05 M$_\odot$ pc^{-3}.

Turning now to the distribution of clump mass vs. velocity dispersion shown in Fig 8(c), a conclusion that can be reached is that lower mass clumps tend to have a lower velocity dispersion. That said, there is a wide range of values even for the low mass clumps, from 0.1 to 0.6 km s^{-1}. High

mass clumps have velocity dispersions in the range 0.5 to 0.8 $\mathrm{km\,s^{-1}}$. Compared to the observed distribution of Heyer & Brunt (2004), the clumps measured here appear to have lower velocity dispersions for their sizes. Velocity dispersions are underestimated by a factor of 2.8 ± 0.67 compared to the scaling law of Larson (1981) and 2.68 ± 0.63 compared to the scaling law of Solomon et al. (1987). We have examined the variation of these factors over time in our simulation and once the clumps have stabilised (by t=0.055) these factors remain remarkably constant. Only during the final collapse of the cloud (from t=0.085) into a single 17,000 $\mathrm{M_\odot}$ clump/core does the velocity dispersion then fit with the Larson and Solomon et al. scaling laws, although taking a different threshold value will change sizes but not the velocity dispersion and hence affect this comparison. In these non-magnetic simulations, under this examination it can be concluded that the TI does not generate large enough velocity dispersions and so there is a need for additional velocity dispersion from other sources. Further simulations will address whether this issue can be rectified with the TI alone, or whether feedback is required. The end-point of our non-magnetic simulation would certainly suggest that the TI in combination with gravitational contraction can reproduce realistic velocity dispersions. A recent observational test would suggest that gravity is the ultimate source of such velocity dispersions (Krumholz & Burkhart 2016).

The gas temperatures in the clumps are on the order of 50-60K. Observationally inferred temperatures are lower than this. This would appear to highlight a limitation of the cooling function and resolution used in this work. Higher resolution and accounting for CO formation is likely to lead to higher densities and lower temperatures but requires complex additions that are not within the scope of this work. We plan to study this in a future work.

As has been demonstrated earlier, a magnetic field suppresses the formation of clumps, so that filamentary structure tends to form instead. With equality of the magnetic pressure and thermal pressure ($\beta = 1.0$), numbers of clumps and filaments form roughly equally. When the magnetic pressure dominates over the thermal pressure, no clumps form. In our simulations, with a low initial density and hence low initial pressure, this occurs even for an average Galactic field strength. In these simulations, the magnetic field is as yet unaffected by the formation of clumps. No field strength enhancement is observed.

It should be noted that under the definition in Table 1 of Bergin & Tafalla (2007), our "clumps" are more like small Bergin & Tafalla clouds in terms of their size and density, but more like Bergin & Tafalla clumps in terms of their mass and velocity dispersion. We do not form structures in these simulations which can be considered as Bergin & Tafalla cores.

6.2 Filaments

Filamentary structures can be described by a Plummer-like function of the form previously described with $p \approx 2$ (Arzoumanian et al. 2011). We now consider whether the filaments formed in our simulations can be described by such a function and if so, with what p value. In Figs 9 and 10 we show the averages of profiles cut across filaments in the $\beta = 1.0$ and 0.1 field cases respectively. These profiles are

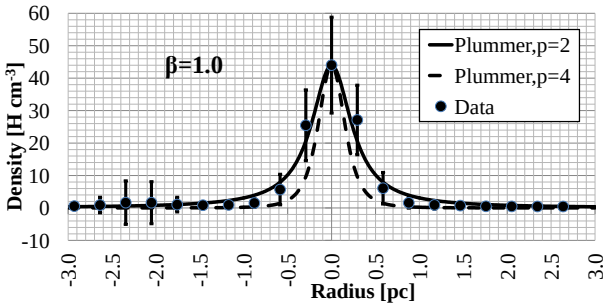

Figure 9. Averaged filament profile across 36 filament cuts in the $\beta = 1.0$ field case with self-gravity, compared to Plummer profiles (solid and dashed lines). The central peak density represents the average central density across these filaments, with the error the standard deviation. The other data points are generated from normalised filament profiles (normalising each filament profile by its central density) in order to obtain these data points that are averages and standard deviations across all 36 filament cuts.

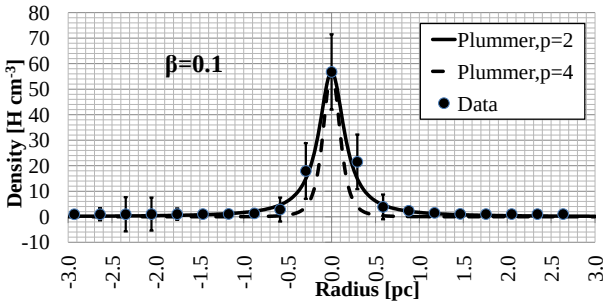

Figure 10. Averaged filament profile across 26 filament cuts in the $\beta = 0.1$ field case with self-gravity, compared to Plummer profiles (solid and dashed lines). The data has been averaged and presented in the same way as Fig. 9.

taken across the cloud at $y = 0$ and values of z ranging across the z range of the cloud, at regular intervals. The central density represents the average from the 36 filament measurements from the $\beta = 1.0$ simulation and 26 filament measurements from the $\beta = 0.1$ simulation. Fewer filament profiles are identified and averaged over in the $\beta = 0.1$ case as there are fewer filaments in the cloud - see column 2 of Fig 6. For both values of β, the error on the central data point is the standard deviation of these central densities. The other data points are averages and the standard deviation calculated after each filament cut has been normalised by its central density in order to allow such a data reduction across filaments with different central densities. In both field cases, we fit the data to Plummer profiles and show that a p=2 profile fits the data better than a p=4 profile for R_{flat} equal to 0.275 pc in the $\beta = 1.0$ case with FWHM $\sim$0.6 pc and R_{flat} equal to 0.15 pc in the $\beta = 0.1$ case with FWHM $\sim$0.35 pc. These values of R_{flat} and FWHM are consistent with other authors (Hennemann et al. 2012; Juvela et al. 2012). For $\beta = 1.0$, taking a filament with central density of $60\,\mathrm{cm^{-3}}$ and central temperature of 50 K (and hence $\mathrm{c_s} \sim 0.8\,\mathrm{km\,s^{-1}}$) from the profile at $y = 0$, $z = 0$, the Jeans length is $\lambda_J = C_s(\pi/G\rho)^{0.5} = 18.4$ pc. For $\beta = 0.1$, the same profile at $y = 0$, $z = 0$ has a filament with central density of $67\,\mathrm{cm^{-3}}$ and central temperature of 50 K, corre-

sponding to a slightly smaller Jeans length $\lambda_J = 17.5\,\mathrm{pc}$. Gravity is not yet affecting the shape and structure of these filaments. Formation is entirely due to the TI. With an enhanced cooling prescription the filaments will cool further and their density will increase. Eventually we expect gravity to dominate the evolution and the filaments will contract further on timescales shorter than the cloud evolution time.

The strength of magnetic field has an effect on filament properties. Comparing Figs 9 and 10, filaments formed in the strong magnetic field case are clearly narrower than in the magnetic/thermal pressure equality case. This could be an effect of time-evolution, but comparing the cloud evolution between $\beta = 1.0$ and $\beta = 0.1$ cases indicates this is not the case. It is more likely due to the more-ordered evolution of the $\beta = 0.1$ case, forming a single corrugated sheet, as opposed to the "bundle" of filaments in the $\beta = 1.0$ case. As for the orientation of the filaments, they are generally perpendicular to the magnetic field, which compares well with observations. Filaments parallel to the field are only flows onto the denser perpendicular filaments in this scenario. In these simulations, the magnetic field is as yet unaffected by the formation of filaments. No field strength enhancement is observed. Further gravitational collapse of the filaments would presumably begin to affect the magnetic field on local filament scales, but larger field strengths measured across the cloud must have a different origin in this scenario.

Temperatures in the filaments are similar to those of the clumps, and in some cases cooler: at the highest densities, the temperatures approach 30 K. Again, these are high compared to the observations, for reasons given in the previous sub-section, but if these are proto-filaments, the continued action of the TI under the influence of gravitational collapse could lead to lower temperatures and higher densities. We hope to be able to examine this in future work.

The velocity profiles across the filaments in both the $\beta = 1.0$ and 0.1 simulations are complex. Different filaments have different central velocities with non-thermal dispersions on these central velocities. Typical filament velocities in the frame of reference of the entire cloud are on the order of $5\,\mathrm{km\,s^{-1}}$ in both field strength cases, with velocities generally directed towards the centre of the cloud. Typical velocity dispersions internally within each filament are on the order of $0.5\,\mathrm{km\,s^{-1}}$. It is important to note three things. Firstly, these internal velocity dispersions are on the order of those measured from observations (Arzoumanian et al. 2011) - TI-driven filament formation can reproduce the "turbulent" velocities measured in filaments (e.g. by Arzoumanian et al. 2013). Secondly, the fact that different filaments have different central velocities, whilst still being part of a larger bundle of filaments or even projection of interconnected sheets highlights that it is now impossible to conclude from observations of filaments with different central velocities that they are separate filaments - in this work they could equally be part of a TI-formed corrugated sheet, non-uniform in density, temperature and velocity. Thirdly, the entirely local TI mechanism drives large-scale, ordered flow on the same scales as that observed and previously considered to be difficult to generate internally. It should also be noted that at the width of the filaments ($\sim$0.3 pc) in this study, a suitably-initialised turbulent velocity scaling relation would likewise predict velocity dispersions of $\sim 0.4\,\mathrm{km\,s^{-1}}$ so the thermal instability is not the only method to obtain such low velocity dispersions.

It should be noted that the clump/filament-formation timescale is far shorter than the diffuse medium evolution timescale. The diffuse cloud initial condition in this work evolves on the scale of tens of Myrs, with a free-fall time t_{ff} $\sim$50 Myrs. The medium remains quiescent and diffuse for the first $\sim$18 Myrs, after which time clumps and filaments characteristic of molecular clouds begin to form out of this medium, which given we start with the lowest possible density initial condition and introduce no external stimulus, is in good agreement with timescales from Galactic scale simulations (section 2.6 of Ostriker et al. 2010; Kim et al. 2011). Hence, the giant molecular cloud can said to have formed at $\sim$18 Myrs. The filaments then reach their final thermodynamic state with high density rapidly after this time (although slow movement of the filaments continues after this time) leading to star formation in the cloud on realistic timescales, in agreement with observations and other numerical work (Clark et al. 2012). In our next work, we consider the injection of stars at this time and the effect of their wind and SN feedback onto the cloud, including timescales of cloud destruction. Given that massive stars will evolve to SN phase on timescales of 3-4 Myrs, the cloud formed in these simulations will be strongly affected, if not destroyed. We examine exactly this evolution and timescale in our next work.

7 CONCLUSIONS

In this paper we explore the idealised evolution of diffuse clouds under the influence of the thermal instability (Field 1965), with magnetic fields and self-gravity and without turbulence. We show that compared to the zero magnetic field case where symmetric stationary clumps rapidly form throughout the cloud, filaments extended perpendicular to the magnetic field lines form as material moves along the field lines. Over a longer time, the filaments continue to move, interconnect and disconnect in both 2D and 3D simulations. At any particular instant, projecting the 3D structure onto a plane generates column density projections that resemble filaments and bundles of filaments in molecular clouds if the plane is parallel to the magnetic field (i.e. **B** is perpendicular to the line of sight). Projected column densities are comparable to observations. Projecting the 3D structure onto a plane perpendicular to the magnetic field (i.e. **B** is parallel to the line of sight), generates clouds remarkably uniform in appearance, circular in projection and not at all filamentary, especially so in the strong field case where material only moves along magnetic field lines and the result is the collapse of a uniform spherical cloud *along this direction*. Column densities are 10$\times$ lower.

The action of the thermal instability in the formation of molecular clouds is not new, but the novelty of this work is in the exploration of the operation of the thermal instability under the influence of the magnetic fields in numerical simulations of diffuse clouds, without external trigger factors e.g. colliding flows or driven turbulence. Clumps and filaments can be formed under the action of the thermal instability alone, without gravity, on realistic timescales with a range of properties comparable to those observed and without the

need to resort to an initial "turbulent" state. In fact, from stationary conditions, velocities such as those observed in molecular clouds are formed in these simulations. This work further emphasizes the fact that the role of the thermal instability and magnetic fields should be fully considered in the formation of molecular clouds. The assumption of isothermal conditions may be missing a significant mechanism.

Limitations, such as neglecting the role of CO, can be interpreted as the reason for not matching all available observational results and future work including the thermal instability should strive to address these limitations. We plan to study the particular role of CO in a future work.

Thermal instability leading to filament formation with or without the influence of gravity does not intensify the magnetic field in our simulations. Other influences are required, for example stellar feedback generating super-sonic, super-Alfvénic motions. This particular question regarding the field-intensifying effect of stellar feedback will be explored in a forthcoming paper that takes these simulations as a starting point and introduces stars and their wind and SNe feedback.

ACKNOWLEDGMENTS

This work was supported by the Science & Technology Facilities Council [Research Grant ST/L000628/1]. We thank the anonymous referee for the positive review and minor suggestions which have improved the manuscript. The calculations for this paper were performed on the DiRAC Facility jointly funded by STFC, the Large Facilities Capital Fund of BIS and the University of Leeds. This facility is hosted and enabled through the ARC HPC resources and support team at the University of Leeds (A. Real, M.Dixon, M. Wallis, M. Callaghan & J. Leng), to whom we extend our grateful thanks. VisIt is supported by the Department of Energy with funding from the Advanced Simulation and Computing Program and the Scientific Discovery through Advanced Computing Program.

REFERENCES

Abergel A., Boulanger F., Mizuno A., Fukui Y., 1994, ApJ, 423, L59
André P. et al., 2010, A&A, 518, L102
André P., Di Francesco J., Ward-Thompson D., Inutsuka S.-I., Pudritz R. E., Pineda J. E., 2014, in Beuther H., Klessen R. S., Dullemond C. P., Henning T., eds, Protostars and Planets VI. University of Arizona Press, Tucson, 914. p. 27, preprint (arXiv:1312.6232)
Arzoumanian D. et al., 2011, A&A, 529, L6
Arzoumanian D., André P., Peretto N., Könyves V., 2013, A&A, 553, id.A119
Bally J., Langer W. D., Stark A. A., Wilson R. W., 1987, ApJ, 312, L45
Balsara D., Ward-Thompson D., Crutcher R. M., 2001, MNRAS, 327, 715
Bastien P., 1983, A&A, 119, 109
Bergin E. A., Tafalla M., 2007, ARAA, 45, 339
Birk G. T., 2000, Physics of Plasmas, 7, 3811
Brunt C. M., 2003, ApJ, 583, 280
Brunt C. M., Heyer M. H., Mac Low M.-M., 2009, A&A, 504, 883
Burkert A., Lin D. N. C., 2000, ApJ, 537, 270
Cambrésy L., 1999, A&A, 345, 965
Chapman N. L., Goldsmith P. F., Pineda J. L., Clemens D. P., Li D., Krčo M., 2011, ApJ, 741, 21
Chini R., Reipurth B., Ward-Thompson D., Bally J., Nyman L.-Å., Sievers A., Billawala Y., 1997, ApJ, 474, L135
Clark P. C., Glover S. C., Klessen R. S., Bonnell I. A., 2012, MNRAS, 424, 2599
Falle S. A. E. G., 1991, MNRAS, 250, 581
Falle S. A. E. G., 2005, Proceedings of the Chicago Workshop on Adaptive Mesh Refinement Methods, Springer Lecture Notes in Computational Science and Engineering (Springer, New York, USA), 41, 235
Federrath C., Roman-Duval J., Klessen R. S., Schmidt W., Mac Low M.-M., 2010, A&A, 512, id.A81
Fiege J. D., Pudritz R. E., 2000, MNRAS, 311, 85
Field G. B., 1965, ApJ, 142, 531
Fischera J., Martin P. G., 2012, A&A, 542, id.A77
Fukue T., Kamaya H., 2007, ApJ, 669, 363
Furuya R. S., Kitamura Y., Shinnaga H., 2014, ApJ, 793, 94
Gnat O., Ferland G. J., 2012, ApJS, 199, article id. 20
Goldreich P., Kwan J., 1974, ApJ, 189, 441
Goldsmith P. F., Heyer M., Narayanan G., Snell R., Li D., Brunt C., 2008, ApJ, 680, 428
Godunov S. K., 1959, Mat. Sbornik, 47, 271
Gómez G. C., Vázquez-Semadini E., 2014, ApJ, 791, article id. 124
Hacar A., Tafalla M., Kauffmann J., Kovács A., 2013, A&A, 554, id.A55
Hartmann L., 2002, ApJ, 578, 914
Hatchell J., Richer J. S., Fuller G. A., Qualtrough C. J., Ladd E. F., Chandler C. J., 2005, A&A, 440, 151
Heitsch F., Stone J. M., Hartmann L. W., 2009, ApJ, 695, 248
Heitsch F., 2013, ApJ, 769, article id. 115
Henshaw J. D., Caselli P., Fontani F., Jiménez-Serra I., Tan J. C., 2014, MNRAS, 440, 2860
Hennebelle P., Banerjee R., Vázquez-Semadini E., Klessen R. S., Audit E., 2008, A&A, 486, L43
Hennebelle P., André P., 2013, A&A, 560, id.A68
Hennemann M., et al. 2012, A&A, 543, id.L3
Heyer M. H., Brunt C. M., 2004, ApJ, 615, L45
Ibáñez-Mejía J. C., Mac Low M.-M., Klessen R. S., Baczynski C., *MNRAS submitted*, preprint (arXiv:1511.05602)
Inoue T., Inutsuka S.-I., 2012, ApJ, 759, article id. 35
Inutsuka S.-I., Miyama S. M., 1992, ApJ, 388, 392
Jiménez-Serra I., Caselli P., Fontani F., Tan J. C., Henshaw J. D., Kainulainen J., Hernandez A. K., 2014, MNRAS, 439, 1996
Johnstone D., Bally J., 1999, ApJ, 510, L49
Juvela M. et al., 2012, A&A, 541, id.A12
Kawamura A. et al., 2009, ApJS, 184, 1
Kim C.-G., Kim W.-T., Ostriker E. C., 2011, ApJ, 743, article id. 25
Kirk H., Klassen M., Pudritz R., Pillsworth S., 2015, ApJ, 802, article id. 75
Könyves V. et al., 2010, A&A, 518, id.L106
Koyama H., Inutsuka S.-I., 2000, ApJ, 532, 980
Koyama H., Inutsuka S.-I., 2002, ApJ, 564, L97

Kritsuk A. G., Norman M. L., 2002, ApJL, 569, L127
Kritsuk A. G., Norman M. L., 2002, ApJL, 580, L51
Krumholz M. R., Burkhart B., 2016, MNRAS accepted, arXiv:1512.03439v2
Kurganov A., Tadmor E., 2000, J. Co. Ph., 160, 241
Larson R. B., 1981, MNRAS, 194, 809
Li D. L., Esimbek J., Zhou J. J., Lou Y.-Q., Wu G., Tang X. D., He Y. X., 2014, A&A, 567, id.A10
Li H., Fang M., Henning T., Kainulainen J., 2013, MNRAS, 436, 3707
Li Z.-Y., Wang P., Abel T., Nakamura F., 2010, ApJ, 720, L26
Lim A. J., Falle S. A. E. G., Hartquist T. W., 2005, ApJ, 632, L91
Mac Low M.-M., Klessen R. S., 2004, Reviews of Modern Physics, 76, 125
Mac Low M.-M., Ossenkopf V., 2000, A&A, 353, 339
Miville-Deschênes M.-A. et al., 2010, A&A, 518, id.L104
Mizuno A., Onishi T., Yonekura Y., Nagahama T., Ogawa H., Fukui Y., 1995, ApJ, 445, L161
Moeckel N., Burkert A., 2015, ApJ, 807, article id. 67
Myers P. C., 2009, ApJ, 700, 1609
Nagai T., Inutsuka S.-I., Miyama S. M., 1998, ApJ, 506, 306
Nagasawa M., 1987, Progress of Theoretical Physics, 77, 635
Nakajima Y., Hanawa T., 1996, ApJ, 467, 321
Nakamura M., Li Z.-Y., 2008, ApJ, 687, 354
Nejad-Asghar M., Ghanbari J., 2003, MNRAS, 345, 1323
Nutter D., Kirk J. M., Stamatellos D., Ward-Thompson D., 2008, MNRAS, 384, 755
Ostriker J., 1964, ApJ, 140, 1056
Ostriker E. C., McKee C. F., Leroy A. K., 2010, ApJ, 721, 975
Padoan P., Juvela M., Goodman A. A., Nordlund Å., 2001, ApJ, 553, 227
Palmeirim P. et al., 2013, A&A, 550, id.A38
Parker E. N., 1953, ApJ, 117, 431
Peretto N. et al., 2012, A&A, 541, id.A63
Pillai T., Kauffmann J., Tan J. C., Goldsmith P. F., Carey S. J., Menten K. M., 2015, ApJ, 799, article id. 74
Planck Collaboration and Bracco, A., 2015, A&A *accepted*, DOI:10.1051/0004-6361/201425044, arXiv:1409.6728
Planck Collaboration, 2015, A&A *accepted*, DOI:10.1051/0004-6361/201425305, arXiv:1411.2271
Plummer H. C., 1911, MNRAS, 71, 460
Pon A., Johnstone D., Heitsch F., 2011, ApJ, 740, article id. 88
Pon A., Toalá J. A., Johnstone D., Vázquez-Semadini E., Heitsch F., Gómez G. C., 2012, ApJ, 756, article id. 145
Porter D., Pouquet A., Woodward P. R., 1994, Phys. Fluids, 6, 2133
Rogers H., Pittard J. M., 2013, MNRAS, 431, 1337
Rogers H., Pittard J. M., 2014, MNRAS, 441, 964
Schneider N. et al., 2012 A&A, 540, id.L11
Schneider S., Elmegreen B. G., 1979, ApJS, 41, 87
Shadmehri M., 2009, MNRAS, 397, 1521
Smith R., Glover S. C. O., Klessen R. S., 2014, MNRAS, 445, 2900
Soler J. D., Hennebelle P., Martin P. G., Miville-Deschênes M.-A., Netterfield C. B., Fissel L. M., 2013, ApJ, 774, article id. 128
Solomon P. M., Rivolo A. R., Barrett J., Yahil A., 1987, ApJ, 319, 730
Stiele H., Lesch H., Heitsch F., 2006, MNRAS, 372, 862
Sugitani K. et al., 2011, ApJ, 734, article id. 63
Toalá J.A., Vázquez-Semadini E., Gómez G.C., 2012, ApJ, 744, article id. 190
Tomisaka K., 2014, ApJ, 785, article id. 24
Umekawa M., Matsumoto R., Miyaji S., Yoshida T., 1999, PASJ, 51, 625
Van Loo S., Falle S. A. E. G., Hartquist T. W., 2010, MNRAS, 406, 1260
Van Loo S., Keto E., Zhang Q., 2014, ApJ, 789, article id. 37
Van Loo S., Tan J. C., Falle S. A. E. G., 2015, ApJ, 800, article id. L11
Vázquez-Semadini E., 1994, ApJ, 423, 681
Vázquez-Semadini E., Gómez G.C., Jappsen A. J., Ballasteros-Paredes J., González R. F., Klessen R. S., 2007, ApJ, 657, 870
VisIt Collaboration, 2012, in "High Performance Visualisation – Enabling Extreme-Scale Scientific Insight", pp. 357-372
Ward-Thompson D. et al., 2010, A&A, 518, id.L92
Whitworth A. P., Ward-Thompson D., 2001, ApJ, 547, 317
Wolfire M. G., Hollenbach D., McKee C. F., Tielens A. G. G. M., Bakes E. L. O., 1995, ApJ, 443, 152
Wolfire M. G., McKee C. F., Hollenbach D., Tielens A. G. G. M., 2003, ApJ, 587, 278
Zuckerman B., Palmer P., 1974, ARA&A, 12, 279